infrastructures

Article

# Quantifying Anisotropic Properties of Old–New Concrete Interfaces Using X-Ray Computed Tomography and Homogenization

**Guanming Zhang** and **Yang Lu** *

Department of Civil Engineering, Boise State University, Boise, ID 83706, USA; guanmingzhang@u.boisestate.edu
* Correspondence: yanglufrank@boisestate.edu; Tel.: +1-208-426-3783

**Abstract:** The interface between old and new concrete is a critical component in many construction practices, including concrete pavements, bridge decks, hydraulic dams, and buildings undergoing rehabilitation. Despite various treatments to enhance bonding, this interface often remains a weak layer that compromises overall structural performance. Traditional design methods typically oversimplify the interface as a homogeneous or empirically adjusted factor, resulting in significant uncertainties. This paper introduces a novel framework for quantifying the anisotropic properties of old–new concrete interfaces using X-ray computed tomography (CT) and finite element-based numerical homogenization. The elastic coefficient matrix reveals that specimens away from the interface exhibit higher values in both normal and shear directions, with normal direction values averaging 33.15% higher and shear direction values 39.96% higher than those at the interface. A total of 10 sampling units along the interface were collected and analyzed to identify the "weakest vectors" in normal and shear directions. The "weakest vectors" at the interface show consistent orientations with an average cosine similarity of 0.62, compared with an average cosine similarity of 0.23 at the non-interface, which demonstrates directional features. Conversely, the result of average cosine similarity at the interface shows randomness that originates from the anisotropy of materials. The average angle between normal and shear stresses was found to be 88.64°, indicating a predominantly orthogonal relationship, though local stress distributions introduced slight deviations. These findings highlight the importance of understanding the anisotropic properties of old–new concrete interfaces to improve design and rehabilitation practices in concrete and structural engineering.

**Keywords:** concrete interface; anisotropic properties; X-ray computed tomography; finite element-based numerical homogenization; mechanical weakness

check for updates

Academic Editor: Patricia Kara De Maeijer

Received: 20 December 2024
Revised: 12 January 2025
Accepted: 13 January 2025
Published: 14 January 2025

**Citation:** Zhang, G.; Lu, Y. Quantifying Anisotropic Properties of Old–New Concrete Interfaces Using X-Ray Computed Tomography and Homogenization. *Infrastructures* **2025**, *10*, 20. https://doi.org/10.3390/infrastructures10010020

**Copyright:** © 2025 by the authors. Licensee MDPI, Basel, Switzerland. This article is an open access article distributed under the terms and conditions of the Creative Commons Attribution (CC BY) license (https://creativecommons.org/licenses/by/4.0/).

## 1. Introduction

Aging civil infrastructure is becoming a critical issue worldwide, particularly in regions where structures, especially those built after World War II, are nearing or exceeding their designed lifespan. Concrete repair, such as overlays and patching, creates interfaces between old and new concrete that are often prone to mechanical weaknesses. These interfaces are heterogeneous, influenced by factors like differential shrinkage, moisture content, and surface preparation, which result in anisotropic properties. Traditional repair methods fail to adequately address these variations, as they assume homogeneity and ignore heterogeneity, which can lead to inaccurate performance predictions [1]. As infrastructure continues to age globally, enhanced methods for quantifying and improving interface performance will be essential for prolonging the lifespan of repairs and ensuring structural integrity [2].

The interface between old and new concrete is a common feature in various construction activities, such as construction joints, where fresh concrete is placed adjacent to previously poured concrete during multistage processes like building large slabs, walls, or bridge piers. It also occurs in renovation and overlay projects, where additional concrete layers are added to pavements, bridge decks, or industrial floors to restore or enhance performance. In rehabilitation efforts, this interface is critical for repairing deteriorated sections of structures like dams, tunnels, or parking garages, as well as in retrofitting buildings to strengthen or adapt them for new uses or modern code compliance. Additionally, it plays a key role in precast concrete applications, such as attaching precast panels to existing frames or foundations. Despite significant advances in bonding techniques, including the use of epoxy resins, surface roughening, and chemical bonding agents, ensuring the long-term mechanical integrity of these interfaces remains a challenge due to differential shrinkage, thermal stresses, and insufficient adhesion, particularly under cyclic loading or environmental exposure [3].

The primary cause of interface cracking between old and new concrete sections is often attributed to shrinkage cracking at the interface [4]. This type of cracking occurs due to differential volume changes when the new concrete dries and shrinks, exerting tensile stresses on the bond between the two layers. If these stresses exceed the tensile strength of the weaker interface, cracks can form [5]. Such interface cracks compromise the structural integrity, leading to potential pathways for moisture infiltration and subsequent degradation through freeze–thaw cycles, chemical reactions, or corrosion of embedded reinforcement [6]. Over time, these damages can significantly weaken the bond strength, reduce load-bearing capacity, and accelerate the overall deterioration of the composite structure [7]. Therefore, it is essential to study the mechanical properties of the old–new concrete interfaces.

Many researchers have made contributions to the old–new concrete interfaces, including qualification of interface properties, influencing factors of interface strength, and establishment of constitutive models with emphasis on the concrete interface or transition zone. Aaleti and Sritharan utilize slant shear test to investigate the behavior at the interface of ultra-high-performance concrete (UHPC), and findings show that adequate shear transfer is achieved with a surface roughness of at least $10^{-3}$ m, irrespective of concrete strength or curing conditions [8]. Ahmed and Aziz studied the shear performance of dry and epoxied joints in precast concrete segmental bridges, finding that epoxied joints offer 25–28% higher shear capacity than dry joints but fail in a brittle manner [4]. Austin, Robins, and Pan reviewed shear bond strength testing methods for concrete repairs, emphasizing the importance of surface preparation and material compatibility. Their work underscores the need for multidimensional approaches to accurately understand adhesion in cementitious repairs [9]. Bentz et al. and Beushausen et al. explore the effects of substrate moisture state on the bond strength and interfacial microstructure of repair materials. The difference is that the former uses neutron and X-ray radiography, while the latter uses the conventional shear test in the laboratory [10,11]. The bond properties between new and old concrete are tested using conventional macroscopic testing methods, and the influence of different factors on the bond strength is investigated [12–14]. Nanoindentation tests and numerical simulations are used in the research of Xiao et al. They focus on the mechanical properties and stress–strain behavior and find that the new mortar matrix and ITZs significantly impact MRAC's mechanical performance, particularly under uniaxial compression and tension [15]. Overall, previous studies have often treated the interface as a homogeneous and isotropic entity for simplicity in calculation and analysis, overlooking its heterogeneous characteristics at the microscopic scale.

Traditional design and test methodologies either assume a homogeneous interface or apply a reduction factor based on empirical data. However, these assumptions introduce uncertainties, as they fail to account for the complex mechanical interactions at the interface [12]. The presence of voids, cracks, and discontinuities at the old–new concrete interface leads to anisotropic behavior that cannot be captured by traditional design approaches. This anisotropy affects the strength, stiffness, and durability of the structure. Moreover, the lack of reliable methods to quantify this weakness from a solid physics and mechanical basis further complicates the problem. This issue is becoming more prominent against the background of aging infrastructure [1].

Micromechanics is an analytical and computational methodology used to study the mechanical behavior of materials at the microstructural level. It examines the interactions between multiple phases—such as grains, inclusions, and interfaces—within a material and investigates how these interactions influence the material's macroscopic mechanical properties. By focusing on microscale features like inclusions, voids, and grain boundaries, micromechanics provides insights into how these elements collectively affect the material's overall performance. This approach enables the prediction of bulk material properties by incorporating intricate microstructural details, effectively bridging the gap between microscale phenomena and macroscopic behavior. Micromechanics has been successfully applied to predict effective properties such as electrical conductivity, thermal conductivity, and elastic moduli [2].

However, traditional micromechanics methods are primarily designed for materials with standard geometries, making their application to random geometries challenging. Randomness in both geometry and the spatial distribution of material phases poses a significant long-term challenge for the application of micromechanics theory to heterogeneous microstructures. Among the various approaches within micromechanics, numerical homogenization has emerged as a state-of-the-art technique for calculating the effective properties of stochastic heterogeneous microstructures. In this work, FEM-based numerical homogenization is conducted due to its advanced computational capability to account for microscale variations. This method provides accurate macroscopic property predictions that capture the complexity and randomness of heterogeneities within the material [16].

Recent advancements in imaging technologies, such as X-ray computed tomography (CT), and computational modeling techniques, like digital image correlation (DIC) and finite element modeling (FEM), present promising solutions for characterizing the interfaces between different phases in concrete materials [17]. X-ray CT provides a non-destructive method to obtain high-resolution 3D images of the internal structure of concrete, allowing for a detailed examination of the distribution of aggregates, voids, and the cement paste matrix [18]. These images offer valuable microstructural data that can be directly integrated into computational models for further analysis. When combined with homogenization techniques, such as those used in micromechanical modeling, these advanced imaging and computational methods enable a more accurate prediction of the mechanical behavior of concrete interfaces under various loading conditions [19]. By employing homogenization, the microstructural data can be used to create effective macroscopic material properties that reflect the heterogeneous nature of concrete, improving the reliability of models predicting concrete performance [20]. Accurate characterization of these interfaces is critical for designing durable, cost-effective repairs, particularly in aging infrastructure subjected to repeated loading and environmental exposure [21]. The integration of X-ray CT data with computational models, therefore, represents a significant advancement in the field of concrete material characterization and repair design, enabling more efficient and precise engineering solutions.

With the research gap in quantifying the anisotropic properties of old–new concrete interfaces, this study aims to propose a method for quantifying the mechanical properties of the old–new concrete interface within a heterogeneous model. By combining X-ray CT scanning technology, homogenization techniques, and data analysis, a new framework is developed to offer deeper insights into the heterogeneous characteristics at the old–new concrete interface. This approach contributes to the understanding of concrete interfaces and holds the potential for advancing future repair and rehabilitation strategies in concrete structures.

## 2. Methodology

The methodology can be expressed as Figure 1.

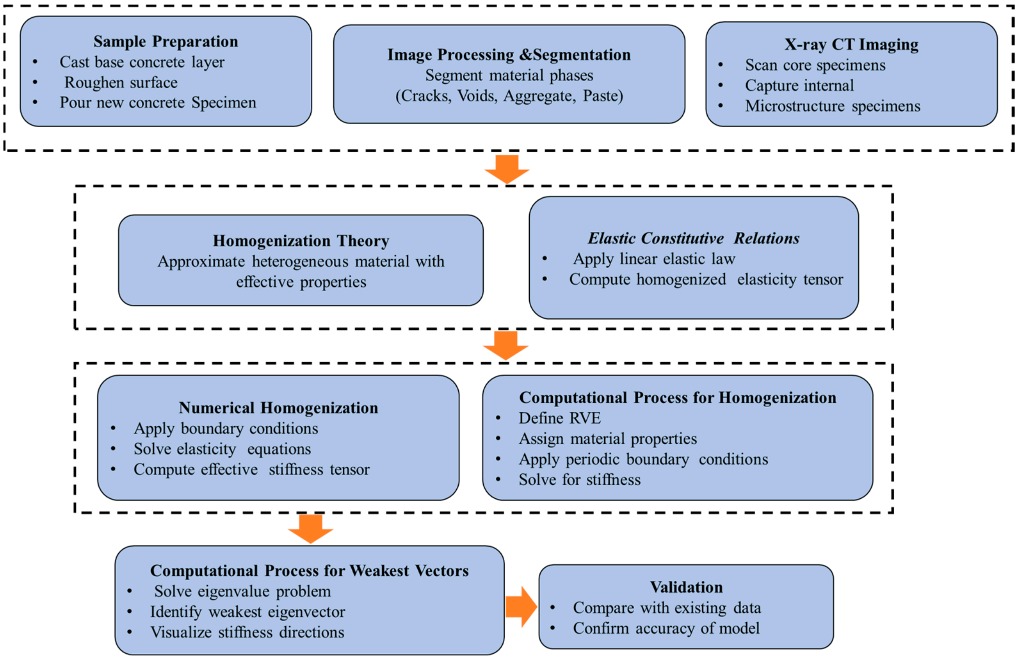

**Figure 1.** Schematic representation of the methodological framework.

As shown in Figure 1, a comprehensive framework is implemented to analyze the mechanical properties of concrete specimens in this study, focusing on the old–new concrete interface. Samples are meticulously prepared to replicate real-world conditions, including casting, surface texturing, and controlled curing. Image processing identifies key material phases, while X-ray CT imaging non-destructively captures the internal microstructure, revealing voids, cracks, and aggregate distribution critical to mechanical behavior. Homogenization theory bridges microscale features with macroscopic behavior, and numerical homogenization solves elasticity equations to determine the effective stiffness tensor. A representative volume element (RVE) with periodic boundary conditions ensures realistic simulations, while eigenvalue analysis identifies the weakest vectors to highlight potential failure directions.

This paper integrates X-ray CT imaging and numerical homogenization to assess the anisotropic properties of the old–new concrete interface, which consists of the following steps.

### 2.1. Sample Preparation

Concrete specimens are prepared to replicate typical conditions found at old–new concrete interfaces in construction [22]. The specimens have a diameter of $2.54 \times 10^{-2}$ m and a length of $2.032 \times 10^{-1}$ m.

The concrete used in this study was a standard mixture designed for structural applications, with a strength grade of C30, in accordance with Ref. [23] for ready-mixed concrete and Ref. [24] for Portland cement. It consisted of Portland cement (Class 42.5), fine aggregate (natural sand with a maximum particle size of 4 mm), coarse aggregate (crushed limestone with a maximum particle size of 20 mm), and potable water. The water-to-cement ratio was set to 0.45 to ensure a target compressive strength of 30 MPa at 28 days. A plasticizer admixture was added at 1.5% of the cement weight to improve workability. The consistency of the fresh concrete was determined using Abram slump test according to Ref. [25], which resulted in a slump value of approximately 75 mm, indicating a rather dry mix with lower workability suitable for the casting process.

The mixture design is summarized in Table 1:

**Table 1.** Mixture design for concrete.

| Ingredient | Specification | Quantity (per $m^3$) | Density ($kg/m^3$) |
|---|---|---|---|
| Cement | Portland cement (Class 42.5) | 371 kg | 3150 |
| Fine Aggregate | Natural sand, max particle size 4 mm | 742 kg | 2650 |
| Coarse Aggregate | Crushed limestone, max size 20 mm | 1166 kg | 2700 |
| Water | Potable water | 166.95 kg | 1000 |
| Admixture | Plasticizer | 1.5% by cement weight | ~1000 (liquid-based) |

The preparation process begins by casting a base layer of concrete to represent the existing structure. After casting, the base layer undergoes an initial curing period of 28 days. This curing allows the base concrete to harden and develop its strength, representing the aged structure in practice. Once the base concrete has gained enough strength, its surface is carefully treated to simulate true construction joint bonding conditions. The surface is roughened using mechanical tools to expose the aggregates and increase mechanical interlocking. These surface treatments mimic field practices used to improve the bond strength between old and new concrete.

After surface preparation, a fresh layer of concrete is mixed and poured over the treated surface to form a composite specimen. The new concrete is placed carefully, ensuring thorough compaction, especially at the interface, to minimize air pockets and potential weak zones. To adequately consolidate the fresh concrete, a mechanical vibrator (Model XYZ, frequency 50 Hz) was used for a duration of 30 s per batch. For smaller or hard-to-reach areas, hand tamping with a steel rod (diameter $10^{-3}$ m) was performed to ensure proper compaction. Specimens were then maintained under controlled water bath curing conditions for a specified period of 28 days, allowing hydration and bonding comparable to field conditions. Once the curing was complete, cylindrical cores were drilled perpendicular to the interface to capture a cross-section of the old–new boundary.

### 2.2. X-Ray CT Imaging

X-ray CT scans are performed on the cores to capture the internal microstructure of the old–new concrete interface [26], highlighting the distribution and morphology of voids, microcracks, aggregates, and the cement matrix.

As shown in Figure 2, voids at the interface are irregularly shaped and unevenly distributed, often forming micro-porous zones that reduce bond strength. Microcracks, frequently oriented along stress concentration paths, vary in width and alignment, contributing to directional mechanical weaknesses. Aggregate particles near the interface show partial embedding, with occasional gaps or weak bonds, while the cement matrix exhibits differences in density and fracture patterns due to variations in hydration and compaction between old and new concrete layers. The interfacial transition zones (ITZs), thin layers surrounding aggregates, display higher porosity and weaker properties compared to the bulk matrix. These microstructural heterogeneities lead to an anisotropic mechanical response, with stress transfer and stiffness varying by direction. The 55-micrometer resolution of X-ray CT scans provides detailed data for quantifying these features, forming a foundation for homogenization analysis. The observed microstructural variations will be further validated in Section 3.

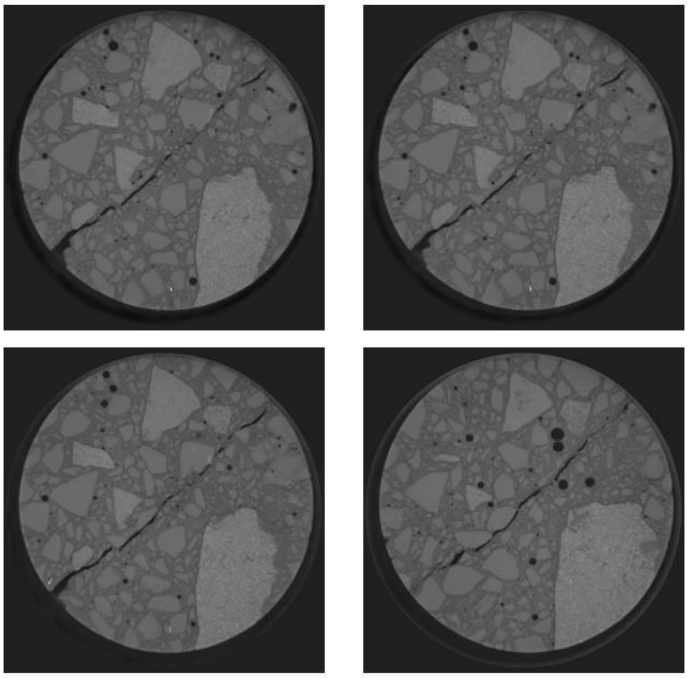

**Figure 2.** X-ray CT micrographs with morphological information of concrete.

### *2.3. Image Processing and Segmentation*

The CT images are processed using image segmentation techniques to differentiate between material phases, including cracks, voids, aggregate, and paste. This step is crucial for generating accurate 3D models of the interface for further analysis [27]. The CT images undergo segmentation to differentiate the primary material phases, including aggregates, paste, voids, and cracks, enabling detailed morphological analysis of the old–new concrete interface. Initial preprocessing involves contrast enhancement and Gaussian filtering to reduce noise and sharpen phase boundaries. A threshold-based binary mask is created to isolate regions of interest, followed by morphological operations to remove noise and refine phase boundaries. Shrink-wrap iterations are applied to enforce circular constraints around the interface, mimicking the geometry observed in actual cross-sections.

Subsequently, grayscale intensity ranges corresponding to each phase are defined for segmentation. Aggregates are segmented within the high-intensity range, paste occupies an intermediate range, and voids and cracks are identified in the lower range. Connected component analysis is performed to classify voids and cracks based on aspect ratios, ensuring precise differentiation of these critical features. The segmented images are stacked to construct comprehensive 3D models for quantifying anisotropic properties, linking microstructural variations to macroscopic mechanical behavior.

As shown in Figure 3, the image on the left represents the segmented version of the original image (Figure 2). The segmented image consists of four grayscale values corresponding to the four material phases: cracks (15), voids (69), paste (129), and aggregate (255). Multiple consecutive segmented images are stacked to create a 3D digital representation of the four-phase concrete. Samples are then extracted at both the interface and non-interface regions to generate multiple subcubes, each measuring 40 × 40 × 40 pixels. The image on the right of Figure 3 illustrates a sampling practice extracting a subcube along the interface region. This method effectively preserves the key features of the multiphase material, such as the distinct characteristics of cracks, voids, paste, and aggregate, while ensuring that the resulting data are sufficiently detailed to provide accurate and reliable predictions of the material's macroscopic properties. It is physically based and represents sensory information from the real world, maintaining the critical microstructural information and capturing the complexity of interface regions. This approach enhances the precision of the analysis without oversimplifying the internal structure of the concrete.

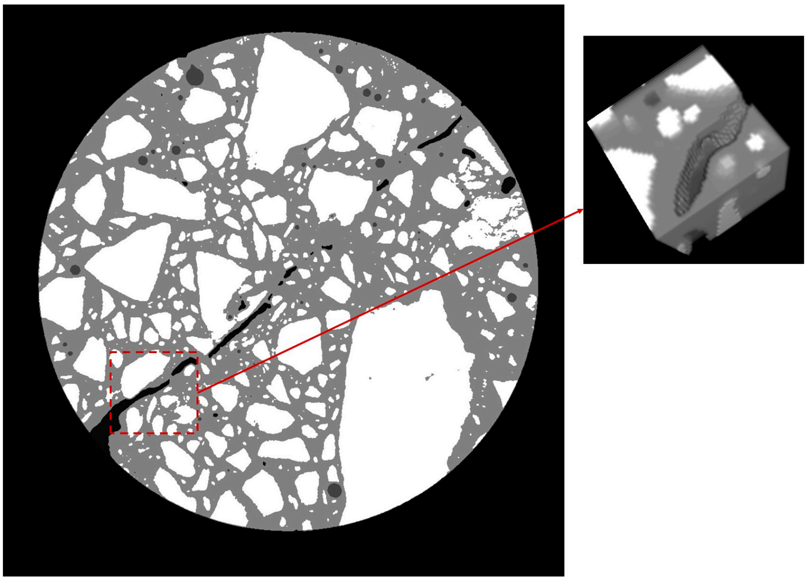

**Figure 3.** Segmented X-ray CT image depicting four-phase material composition.

In the model development process for this study, a simplified tetrahedral mesh was generated to represent the heterogeneous material microstructure, following the approach described by Ref. [28], which involves topological and geometric data processing to create meshes with consistent interfaces between aggregates and cement paste.

### 2.4. Finite Element-Based Numerical Homogenization

It is noteworthy that homogenization theory approximates a heterogeneous material as an equivalent homogeneous material with effective properties [21]. The fundamental principle is to establish a relationship between the microscopic behavior of individual phases and the macroscopic response of the composite material [27]. The effective properties are typically represented by the elastic modulus tensor, which relates stress and strain on the macroscopic scale.

The method of asymptotic numerical homogenization with periodic boundary conditions is one of the most effective approaches to obtaining the effective homogenized stiffness matrix of a heterogeneous elastic material. In this finite element-based approach, six boundary conditions are applied to a representative volume element (RVE), which is modeled with detailed micro-/mesoscale multi-phasic constituents, to calculate the homogenized elastic properties of the RVE [29].

The elastic behavior of a homogeneous or pseudo-homogeneous material is described by the linear elastic constitutive law:

$$\sigma = C{:}\varepsilon \tag{1}$$

where

$\sigma$ is the stress tensor.

C is the elastic modulus tensor (homogenized elasticity tensor).

$\epsilon$ epsilon$\epsilon$ is the strain tensor.

In multiphase materials, the effective elastic modulus tensor C can be computed using periodic boundary conditions and a systematic approach involving multiple load cases [26].

The first step in the computational process is to define a representative volume element (RVE) that captures the essential features of the microstructure. The RVE should be large enough to represent the statistical behavior of the material while being small enough for computational feasibility.

Once the RVE is defined, material properties must be assigned to each constituent phase. These properties include Young's modulus, Poisson's ratio, and other relevant mechanical properties, which can vary significantly between different phases.

Boundary conditions play a crucial role in the homogenization process. Periodic boundary conditions are often applied to ensure consistency across the RVE. This involves establishing relationships between the displacements and tractions on corresponding boundaries. The periodic boundary condition can be expressed as follows:

$$u_d(x) = u_s(x + L) \tag{2}$$

where

$u_d$ and $u_s$ are the displacement vectors at the destination and source boundaries, respectively.

L is the position vector connecting the source and destination boundaries.

Additionally, the continuity of tractions across adjacent RVE boundaries is enforced:

$$T_1 = T_2 \tag{3}$$

where $T_1$ and $T_2$ are the traction vectors at the adjacent boundaries—these conditions simulate the behavior of homogeneous materials and are crucial for calculating the equivalent elastic modulus matrix.

To compute the homogenized elasticity tensor C, six different load cases are applied, covering standard deformation modes in three axial and three shear directions. Each load case prescribes a non-zero component of the average strain tensor while keeping the others at zero. The average traction vector for each load case is used to construct C.

The effective stiffness tensor can be obtained by solving the following relation in each load case:

$$T = C{:}\ \epsilon \tag{4}$$

where T is the average traction vector corresponding to the applied strain.

The elastic constitutive law for a homogeneous or pseudo-homogeneous material is written as follows:

$$\begin{bmatrix} \sigma_{avg,11} \\ \sigma_{avg,12} \\ \sigma_{avg,13} \\ \sigma_{avg,14} \\ \sigma_{avg,15} \\ \sigma_{avg,16} \end{bmatrix} = D_{avg}\cdot \begin{bmatrix} \epsilon_{avg,11} \\ \epsilon_{avg,12} \\ \epsilon_{avg,13} \\ \epsilon_{avg,14} \\ \epsilon_{avg,15} \\ \epsilon_{avg,16} \end{bmatrix} \tag{5}$$

where $D_{avg}$ is the homogenized elasticity tensor. To find the components of the homogenized elasticity tensor using the periodic boundary conditions, six load cases are required. In each load case, one strain component is prescribed while the others are zero.

After obtaining the heterogeneous elastic matrix, this work proposes a novel method to assess the anisotropic properties of old–new concrete, addressing the current gap in accurate quantification. This approach provides valuable insight for better understanding the interface between old and new concrete. The core of the analysis lies in solving the eigenvalues and eigenvectors of the material, identifying its stiffness properties in different directions, and particularly focusing on the "weakest" eigenvector associated with the smallest eigenvalue. This analysis plays a key role in understanding the material's response under various stress and strain conditions, especially in the evaluation of elastic properties of multiphase or complex materials.

Given a 6 × 6 constitutive matrix C, it can be represented as follows:

$$\begin{bmatrix} C_{11} & C_{12} & C_{13} & C_{14} & C_{15} & C_{16} \\ C_{21} & C_{22} & C_{23} & C_{24} & C_{25} & C_{26} \\ C_{31} & C_{32} & C_{33} & C_{34} & C_{35} & C_{36} \\ C_{41} & C_{42} & C_{43} & C_{44} & C_{45} & C_{46} \\ C_{51} & C_{52} & C_{53} & C_{54} & C_{55} & C_{56} \\ C_{61} & C_{62} & C_{63} & C_{64} & C_{65} & C_{66} \end{bmatrix} \tag{6}$$

This matrix C characterizes the material's anisotropic stiffness properties, which is crucial for understanding how the material responds to stress and strain in different directions.

### 2.5. Weakest Vector Index

The homogenization method effectively addresses the issue of macroscopic representation of the elastic modulus in heterogeneous models. To gain a deeper understanding and evaluation of the directional properties of the elastic modulus at the old–new concrete interface under heterogeneous conditions, this study introduces a new index in this subsection called the "weakest vector."

The introduction of this index begins with the definition of the eigenvector, and the eigenvalue problem is solved as follows:

$$\mathrm{Cv} = \lambda \mathrm{v} \tag{7}$$

where λ represents the eigenvalue, and v is the corresponding eigenvector. The eigenvalue λ represents the stiffness of the material in the direction defined by v. Larger eigenvalues indicate higher stiffness, while smaller eigenvalues represent lower stiffness or higher compliance.

After obtaining all the eigenvalues and eigenvectors, the smallest eigenvalue $\lambda_{\mathrm{min}}$ and its corresponding eigenvector $\mathrm{v}_{\mathrm{weak}}$ are extracted. This direction, $\mathrm{v}_{\mathrm{weak}}$, is referred to as the "weakest direction", representing the direction in which the material is most susceptible to deformation. This is mathematically expressed as follows:

$$\lambda_{min} = min(\lambda_1, \lambda_2, \ldots, \lambda_6),\ v_{weak} = vi,\ where\ \lambda_i = \lambda_{min} \tag{8}$$

To visualize stiffness in different directions, the eigenvectors are scaled by their eigenvalues and plotted in 3D space. The length of each eigenvector corresponds to its eigenvalue, illustrating the material's relative stiffness in that direction. The weakest eigenvector is highlighted with a distinctive color, with annotations indicating its eigenvalue and index.

This analytical method is crucial for assessing the material's response under complex stress conditions and identifying potential weaknesses. Studying the weakest stiffness direction provides deeper insights, enabling engineers and researchers to better assess the structural performance and safety of the material.

### 2.6. Validation

The Self-Consistent Scheme (SCS) is a well-established micromechanical model used to predict the effective elastic properties of heterogeneous materials [30]. It assumes that each phase in the composite behaves as though embedded in an effective medium, which is itself an unknown property to be determined. Current research has demonstrated the validity of comparing the Self-Consistent Scheme (SCS) with FEM analysis for characterizing composite material properties, showing that FEM-based calculations can be reliably verified using SCS [31].

The iterative process ensures that the strain field within each inclusion satisfies the self-consistency condition. The effective stiffness tensor $C_{eff}$ is computed by solving the following relation:

$$C_{eff} = C_m + \sum_{i=1}^{n} v_i (C_i - C_m) A_i \tag{9}$$

where $C_m$ is the stiffness tensor of the matrix, $C_i$ is the stiffness tensor of inclusion i, $v_i$ is the volume fraction of phase i, and $A_i$ is the strain concentration factor derived from the Eshelby tensor.

As shown in Figure 4, to validate our adopted finite element-based homogenization method, this work applied the SCS to a model containing two phases: a matrix with Young's modulus $E_m = 7 \times 10^{10}$ Pa and Poisson's ratio $\nu_m = 0.25$ and spherical inclusions with $E_i = 2 \times 10^{11}$ Pa and $\nu_i = 0.3$. The inclusion, with a fraction of 11.31%, is randomly distributed within a cubic domain with an edge length of $10^{-3}$ m. The material properties and phase geometry are consistent across both the SCS and finite element models.

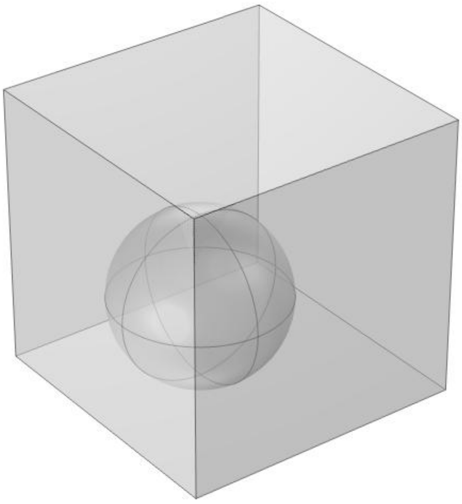

**Figure 4.** Geometry input for SCS and FEM methodologies.

The effective stiffness tensors derived from the SCS and FEM approaches are compared below. For brevity, the two 6 × 6 matrices are as follows:

As shown in (10) and (11), the results reveal overall consistency between the two methods, particularly along the diagonal terms ($C_{11}$, $C_{22}$, $C_{33}$), where the relative differences are less than 2% (e.g., $C_{11}$ = 241.29 from SCS vs. 237.14 from FEM, yielding a relative error of 1.7%). Off-diagonal terms ($C_{12}$, $C_{13}$, etc.) and shear components ($C_{44}$, $C_{55}$, $C_{66}$) show minor discrepancies, with maximum absolute differences of approximately $4 \times 10^9$ Pa in shear moduli. The observed negative off-diagonal values in the elastic matrix can be attributed to the intrinsic heterogeneity of the composite material and the complex interfacial interactions between the two phases, reflecting the inherent anisotropic mechanical coupling and physical behavior of the system.

$$\begin{bmatrix} 241.29 & 101.82 & 101.82 & 0.00 & 0.00 & 0.00 \\ 101.82 & 241.29 & 101.82 & 0.00 & 0.00 & 0.00 \\ 101.82 & 101.82 & 241.29 & 0.00 & 0.00 & 0.00 \\ 0.00 & 0.00 & 0.00 & 70.63 & 0.00 & 0.00 \\ 0.00 & 0.00 & 0.00 & 0.00 & 70.63 & 0.00 \\ 0.00 & 0.00 & 0.00 & 0.00 & 0.00 & 70.63 \end{bmatrix} \tag{10}$$

$$\begin{bmatrix} 237.14 & 97.65 & 97.65 & -0.29 & -0.46 & -0.63 \\ 97.65 & 237.14 & 97.65 & -0.37 & -0.21 & -0.49 \\ 97.65 & 97.65 & 237.14 & -0.41 & -0.43 & -0.36 \\ -0.29 & -0.37 & -0.41 & 69.06 & 0.82 & 0.61 \\ -0.46 & -0.21 & -0.43 & 0.82 & 69.06 & 0.78 \\ -0.63 & -0.49 & -0.36 & 0.61 & 0.78 & 69.06 \end{bmatrix} \tag{11}$$

Compared with statistical homogeneity, the validation confirms the robustness of the finite element-based homogenization approach combined with our selected component properties. The FEM results demonstrate its capability to accurately predict the effective elastic moduli of multiphase, heterogeneous materials with random microstructures, validating its use in homogenization studies for random composite materials.

## 3. Results and Discussion

The results of numerical evaluation reveal a strong correlation between the quantified anisotropy of the elastic modulus and the microstructural features of the concrete, particularly in the interface regions. The stiffness tensors exhibit notable directional dependence, with reduced stiffness observed perpendicular to the interface. This reduction is closely tied to microstructural characteristics identified through X-ray CT scans, such as the distribution and morphology of voids, microcracks, aggregates, and the cement matrix.

Voids at the interface are irregularly shaped and unevenly distributed, forming microporous zones that weaken bond strength. Microcracks, aligned along stress concentration paths, vary in width and orientation, introducing directional weaknesses in mechanical response. Aggregates near the interface show partial embedding with occasional gaps or weak bonds, while the cement matrix displays variations in density and fracture patterns due to differences in hydration and compaction between old and new concrete layers. The interfacial transition zones (ITZs), thin, porous layers surrounding aggregates, further contribute to directional stiffness variability. These microstructural heterogeneities, quantified at a resolution of $5.5 \times 10^{-5}$ m using X-ray CT, underlie the observed anisotropic behavior.

The findings emphasize the critical role of interface heterogeneity in governing mechanical behavior, challenging traditional design assumptions that neglect anisotropic effects. The current reliance on empirical reduction factors fails to capture the true mechanical response of the interface, potentially leading to inaccuracies in structural performance estimation. These microstructural observations provide a robust basis for homogenization analysis, bridging the gap between detailed features and macroscopic anisotropy.

### *3.1. Results of Elastic Constitutive Matrix*

Constitutive relations in linear elasticity are given by the generalized Hooke law, which linearly relates the stress and strain tensors to the elasticity and/or compliance tensors. The coefficients of these linear relations are the elastic and/or compliance moduli, as calculated in this subsection [32].

The elements of matrix C reveal key insights into the material's anisotropic properties at the old–new concrete interface. The diagonal terms $C_{11}$, $C_{22}$, and $C_{33}$ represent the material's stiffness along the x, y, and z axes, indicating its resistance to axial deformation. Higher values highlight the primary load-bearing capabilities. The off-diagonal terms $C_{12}$, $C_{13}$, and $C_{23}$ capture anisotropic coupling, where stress in one direction induces strain in another, reflecting the transitional properties of the old–new concrete interface. The shear terms $C_{44}$, $C_{55}$, and $C_{66}$ describe resistance to shear deformation in the yz, xz, and xy planes, providing insights into interfacial bonding and structural cohesion under shear loads [28].

Using the homogenized model derived from numerical simulations, the effective elastic constitutive matrix C is calculated based on segmented X-ray CT images. In this paper, a total of 18 samples are calculated with a size of 40 × 40 × 40 for each sample. According to the sampling position, it can be divided into interface position samples and non-interface position samples.

The matrix C is determined by applying six prescribed load cases, each inducing a unique strain component. This approach enables us to obtain a complete 6 × 6 matrix of stiffness coefficients, capturing the interactions between stress and strain in multiple directions. Selected components of the calculated C matrix are presented in the following tables.

As shown in (12), the elasticity matrix of the non-interface position reveals that the diagonal elements represent axial stiffness along the principal directions (x, y, z), with higher values indicating greater stiffness. In the non-interface position matrix, the high values in axial directions, especially $C_{11}$ = 31,937.09, $C_{22}$ = 31,193.96, and $C_{33}$ = 35,270.82, suggest that this region is generally stiffer due to better compaction and fewer microstructural voids in the old–new concrete interface. This uniform axial stiffness across principal directions is typical in regions where the concrete is well-bonded.

$$\begin{bmatrix} 31{,}937.09 & 9165.88 & 9207.04 & 5.61 & 142.71 & 89.06 \\ 9165.88 & 31{,}193.96 & 9332.21 & 256.75 & 22.84 & 182.96 \\ 9207.04 & 9332.21 & 35{,}270.82 & 404.62 & 198.80 & 100.80 \\ 5.61 & 256.75 & 404.62 & 11{,}518.02 & 126.12 & 28.12 \\ 142.71 & 22.84 & 198.80 & 126.12 & 11{,}437.41 & 30.72 \\ 89.06 & 182.96 & 100.80 & 28.12 & 30.72 & 11{,}141.91 \end{bmatrix} \tag{12}$$

As shown in (13), in contrast, the interface position matrix shows lower values across the diagonal, particularly $C_{11}$ = 18,970.84 and $C_{22}$ = 14,562.60, suggesting that the material is more compliant or less stiff in these directions. This is likely due to weaker bonding or microstructural defects, such as voids or cracks.

$$\begin{bmatrix} 18{,}970.84 & 6042.31 & 5695.41 & -26.32 & 527.61 & 4527.15 \\ 6042.31 & 14{,}562.60 & 4885.64 & -388.06 & 128.25 & 4420.14 \\ 5695.41 & 4885.64 & 33314.93 & -391.05 & 734.93 & 1998.46 \\ -26.32 & -388.06 & -391.05 & 7625.52 & 2883.81 & 131.13 \\ 527.61 & 128.25 & 734.93 & 2883.81 & 8721.25 & -25.82 \\ 4527.15 & 4420.14 & 1998.46 & 131.13 & -25.82 & 7737.81 \end{bmatrix} \tag{13}$$

Examining the off-diagonal elements reveals insights into shear and coupling effects between different axes. Higher off-diagonal values typically suggest stronger bonding and resistance to deformation in off-axis directions, while lower or negative values may imply structural weaknesses or anisotropy. In the non-interface position matrix, many off-diagonal elements are relatively small, with values close to zero or low magnitudes (e.g.,

$C_{14}$ = 5.61, $C_{13}$ = 9207.04), indicating minimal shear coupling or anisotropy effects between the principal axes. This consistency aligns with a well-bonded, isotropic-like region.

In the interface position matrix, however, the off-diagonal terms are more variable, with some significantly negative values (e.g., $C_{14} = -26.32$, $C_{24} = -388.06$) and others with larger magnitudes (e.g., $C_{15}$ = 527.61, $C_{35}$ = 734.93). The presence of negative values suggests internal stresses or localized anisotropy, likely due to structural weaknesses at the interface. These irregularities indicate greater anisotropic behavior and less cohesive bonding between phases in the interface position.

Overall, the non-interface position has consistently higher values in both axial and off-diagonal terms, indicating a generally stiffer and more isotropic behavior. This reflects a stronger bond at the old–new concrete interface, with minimal voids or cracks. In contrast, the interface position matrix shows significant variability, with lower and negative values in the off-diagonal terms, indicating anisotropic behavior where certain directions are more compliant. These variations are likely due to defects such as cracks, voids, or weak bonding regions, making this position more susceptible to deformation in specific directions.

In practical terms, the non-interface position is likely to resist load application more effectively in all directions, maintaining structural integrity under stress. The interface position, however, suggests potential failure zones, particularly when loads are applied along or perpendicular to planes where defects reduce stiffness.

The calculated constitutive matrix reveals significant anisotropy due to the heterogeneous nature of the old–new concrete interface. The variation in stiffness across different directions, with distinct values for $C_{11}$, $C_{22}$, and $C_{33}$, highlights the directional stiffness characteristics of the interface. This anisotropic behavior arises from the presence of voids, microcracks, and bonding inconsistencies within the interface region.

Additionally, the off-diagonal terms indicate substantial coupling between axial and shear deformations, a typical feature in composite materials with uneven bonding. These shear coupling effects underscore the complex response of the interface when subjected to multi-directional loading, reflecting its non-uniform and transitional nature. Together, these observations characterize the old–new concrete interface as a zone of variable stiffness and intricate mechanical behavior [33].

### *3.2. Calculation and Visualization of Weakest Vectors*

As described in Section 2, the process of calculating the "weakest vector" in a constitutive matrix analysis begins with the definition of eigenvalues and eigenvectors.

To obtain the eigenvalues $\lambda_i$ and corresponding eigenvectors of C, the matrix equation is solved:

$$C \times v_i = \lambda_i \times v_i \tag{14}$$

where each $\lambda_i$ is an eigenvalue, and each $v_i$ is the corresponding eigenvector. This computation produces a diagonal matrix of eigenvalues and a matrix of eigenvectors, where each column in the eigenvector matrix corresponds to an eigenvector associated with an eigenvalue in the eigenvalue matrix. Extracting the eigenvalues as a vector allows for further analysis of the material's directional properties.

The "weakest vector" is identified as the eigenvector associated with the smallest eigenvalue of C. This smallest eigenvalue represents the minimum response or stiffness in the direction of its corresponding eigenvector, making it the "weakest" direction in the material. Specifically, this work identifies the minimum eigenvalue $\lambda\text{min} = \min\{\lambda_1, \lambda_2, \ldots, \lambda_6\}$ and finds the index $\text{idxweakest} = \text{argmin}\{\lambda_1, \lambda_2, \ldots, \lambda_6\}$ to locate the corresponding eigenvector $\text{vweakest} = \text{vidxweakest}$.

To visualize the eigenvalues and eigenvectors, each eigenvector can be scaled proportionally to its eigenvalue, with length and thickness adjusted to show the relative magnitude of each eigenvalue. The scaling factor for each eigenvector is calculated as follows:

$$\lambda_i^{\text{scaled}} = 1 + 4 \cdot \frac{\lambda_i - \min(\{\lambda\})}{(\{\lambda\}) - \min(\{\lambda\})} \tag{15}$$

This proportional scaling highlights variations among eigenvalues, enabling a clear comparison of the material's characteristic directions. The "weakest vector", marked distinctly, stands out as the vector of minimal response, signifying the direction in which the material exhibits the least resistance. This analysis can provide valuable insights into material behavior under different forces and is widely applicable in fields like materials science and mechanical engineering, where understanding directional responses to stress and strain is essential.

As illustrated in Figures 5 and 6, to investigate the anisotropic properties of the old–new concrete interface, the weakest vectors are visualized. The first three components of each weakest vector correspond to the direction of minimum resistance under normal stress and are represented by a red arrow with a solid line. Conversely, the last three components of the weakest vector indicate the direction of minimum resistance under shear stress, denoted by a blue arrow with a dashed–dotted line.

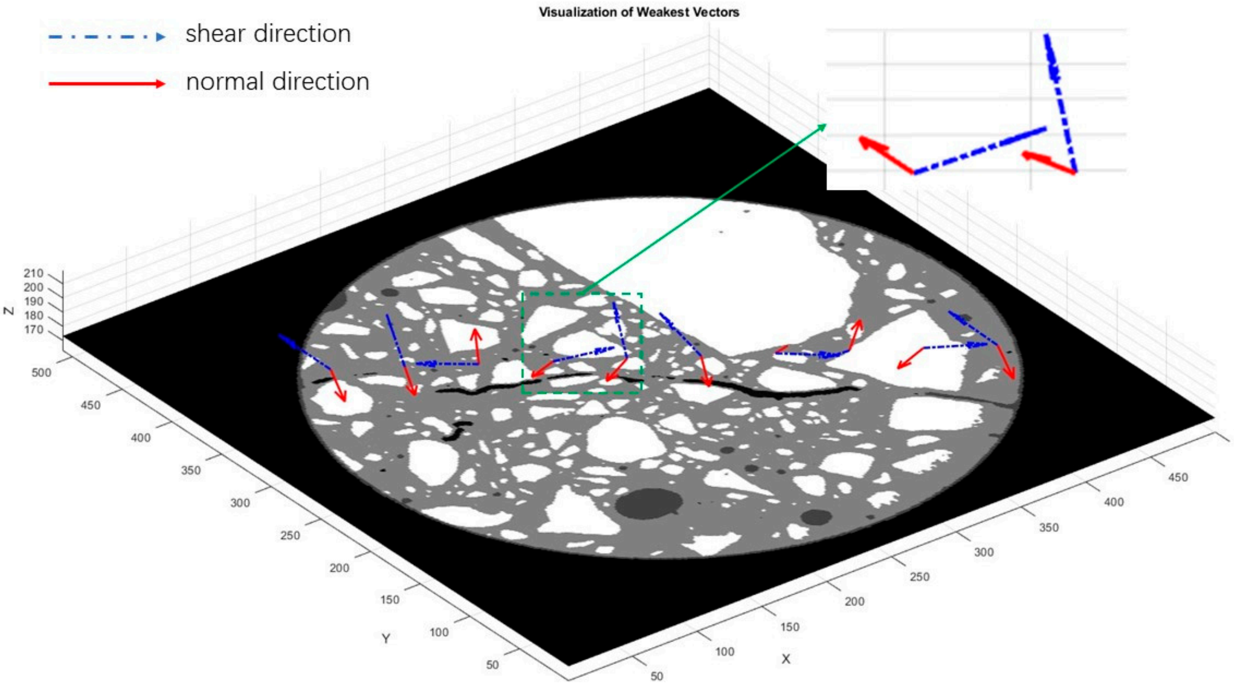

**Figure 5.** Three-dimensional visualization of weakest vectors in old–new concrete (solid lines indicate normal direction; dashed–dotted lines indicate shear direction).

The angles between the weakest normal stress direction and the corresponding weakest shear stress direction are calculated for ten specific vector pairs. The computed angles are as follows: 101.38°, 85.68°, 73.11°, 96.41°, 80.26°, 91.82°, 72.37°, 85.27°, 103.42°, and 96.68°. These values indicate a variation in the relative orientation between the normal and shear stress components across the sampled pairs. The mean angle is determined to be 88.64°, reflecting a predominantly orthogonal relationship with some deviation due to local stress distributions.

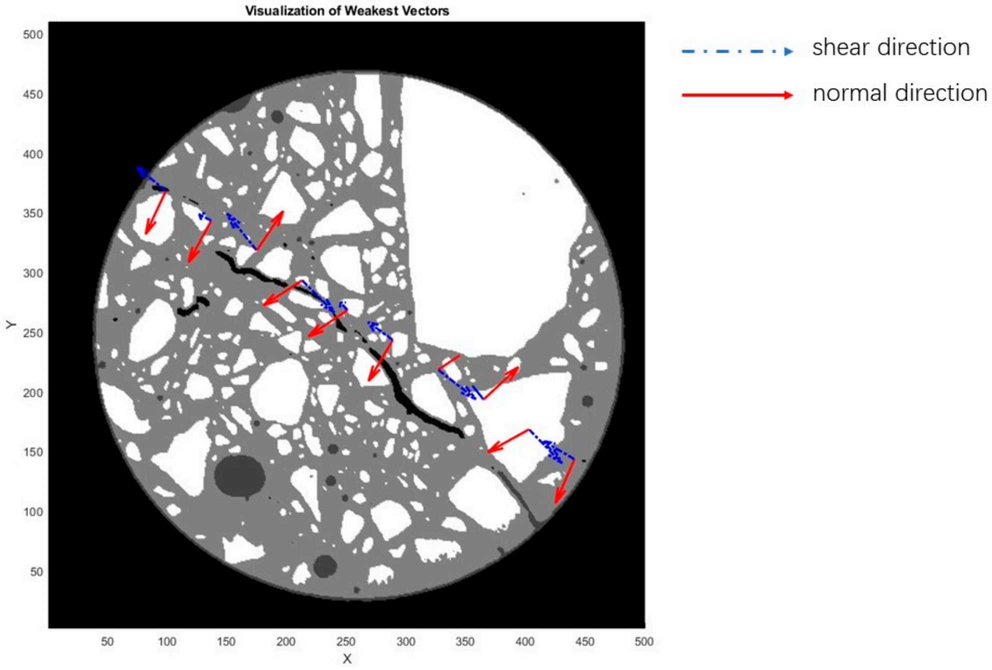

**Figure 6.** Two-dimensional visualization of weakest vectors in old–new concrete (solid lines represent normal direction; dashed–dotted lines represent shear direction).

### *3.3. Similarity Analysis of Weakest Vectors*

Based on the visualization of the weakest vectors, it is found that there are similarities between these vectors, which might show the properties of the interface of old–new concrete. To analyze the anisotropic properties of the interface deeply, the similarity is quantified in this subsection.

As shown in (16), based on the calculated elastic matrix, we can obtain the "weakest vectors" of interface positions. Each column represents a vector. This work resamples 10 cubic specimens at the interface, each measuring 40 × 40 × 40, at various interface positions. For each sample, the "weakest vectors" are computed, representing the direction of minimal material resistance. These "weakest vectors" are then assembled into a matrix, termed the "weakest vector matrix". This matrix has dimensions of 6 × 10, where each column corresponds to the vector of an individual sample.

$$\begin{bmatrix} -0.1079 & -0.1036 & 0.0142 & -0.0296 & -0.0752 & -0.1148 & 0.0126 & 0.0596 & -0.0309 & -0.0916 \\ -0.2310 & -0.1894 & 0.0211 & -0.0193 & -0.0508 & -0.1945 & 0.0085 & 0.0556 & -0.0172 & -0.2131 \\ -0.0004 & 0.0151 & 0.0012 & 0.0092 & 0.0134 & 0.0076 & -0.0049 & -0.0024 & 0.0057 & -0.0080 \\ -0.5979 & -0.2465 & -0.6190 & 0.6719 & -0.1405 & -0.5026 & 0.7869 & -0.5626 & 0.6900 & -0.6347 \\ 0.4888 & 0.1254 & 0.7744 & -0.6686 & 0.1604 & 0.3620 & -0.6160 & 0.7053 & -0.7074 & 0.3722 \\ 0.5819 & 0.9363 & -0.1289 & 0.3165 & 0.9727 & 0.7518 & -0.0323 & -0.4236 & 0.1487 & 0.6361 \end{bmatrix} \tag{16}$$

The calculation process implements a method to compute a cosine similarity matrix for a set of vectors, each representing a "weakest vector". Cosine similarity is a measure used to evaluate the directional alignment between two non-zero vectors by calculating the cosine of the angle between them. This measure ranges from $-1$ to 1, where a value of 1 indicates perfect alignment in the same direction, $-1$ indicates alignment in opposite directions, and 0 indicates orthogonality or complete lack of alignment.

Initially, the vectors are defined and organized into a matrix, where each column corresponds to an individual vector. A square matrix is then created to store the cosine similarity values, with dimensions equal to the number of vectors. The calculation of cosine similarity between each unique pair of vectors, including each vector with itself, follows by retrieving vectors a and b and computing the similarity using the formula:

$$\cos\_\mathrm{sim}(a, b) = \frac{a \cdot b}{||a|| \times ||b||} \tag{17}$$

where a·b denotes the dot product of the two vectors, and $||a||$ and $||b||$ are their magnitudes. The computed similarity is stored symmetrically in the matrix since cosine similarity is a symmetric measure.

As shown in (18), further analysis is then performed on the cosine similarity matrix. The average cosine similarity is calculated by taking the absolute values of the matrix entries, excluding the diagonal elements, and averaging them. The average similarity at non-interface positions is 0.23, compared to 0.62 at interface positions. This indicates that the "weakest vectors" at the interface demonstrate greater directional consistency. This metric indicates the general alignment across the set of vectors. Additionally, the variance of these similarity values is computed to reveal the diversity in orientation. In this case, the variance is 0.11, which shows that these "weakest vectors" have minimal fluctuation. The low variance suggests homogeneity in alignment. This phenomenon is consistent with the results observed in X-ray CT images. The interface between the new and old concrete has obvious directionality as a whole, which leads to the convergence of the weakest normal stress and shear stress in direction. However, due to the local heterogeneity, the similarity of the weakest vector only reaches 0.62. It can be inferred that if the size of the sampling unit is larger or the heterogeneity of the interface position is lower, the similarity will increase.

$$\begin{bmatrix} 1.0000 & 0.8084 & 0.6672 & -0.5367 & 0.7482 & 0.9723 & -0.7937 & 0.4153 & -0.6645 & 0.9907 \\ 0.8084 & 1.0000 & 0.1235 & 0.0537 & 0.9831 & 0.9221 & -0.3045 & -0.1862 & -0.1130 & 0.8485 \\ 0.6672 & 0.1235 & 1.0000 & -0.9752 & 0.0837 & 0.4888 & -0.9596 & 0.9510 & -0.9949 & 0.5933 \\ -0.5367 & 0.0537 & -0.9752 & 1.0000 & 0.1095 & -0.3346 & 0.9298 & -0.9865 & 0.9850 & -0.4673 \\ 0.7482 & 0.9831 & 0.0837 & 0.1095 & 1.0000 & 0.8786 & -0.2422 & -0.2272 & -0.0625 & 0.7853 \\ 0.9723 & 0.9221 & 0.4888 & -0.3346 & 0.8786 & 1.0000 & -0.6459 & 0.2019 & -0.4842 & 0.9840 \\ -0.7937 & -0.3045 & -0.9596 & 0.9298 & -0.2422 & -0.6459 & 1.0000 & -0.8622 & -0.9529 & -0.7523 \\ 0.4153 & -0.1862 & 0.9510 & -0.9865 & -0.2272 & 0.2019 & -0.8622 & 1.0000 & -0.9529 & 0.3329 \\ -0.6645 & -0.1130 & -0.9949 & 0.9850 & -0.0625 & -0.4842 & 0.9734 & -0.9529 & 1.0000 & -0.6003 \\ 0.9907 & 0.8485 & 0.5933 & -0.4673 & 0.7853 & 0.9840 & -0.7523 & 0.3329 & -0.6003 & 1.0000 \end{bmatrix} \tag{18}$$

Finally, the process identifies, for each vector, the maximum cosine similarity with any other vector, excluding itself, thereby indicating the closest directional alignment among the set. According to computation, the average value of maximum cosine similarity is 0.99, showing that every "weakest vector" has at least one other vector that has the same direction as itself. This phenomenon further confirms that the "weakest vectors" at the interface between new and old concrete have a high similarity in direction.

### *3.4. Discussion*

The heterogeneous nature of the old–new concrete interface is a critical factor contributing to its anisotropic behavior in many rehabilitation projects. Due to differential shrinkage, thermal expansion, and the inherent incompatibilities between the old and new concrete layers, the interface exhibits directional variations in properties such as stiffness, strength, and crack resistance [3,4]. These variations are not uniformly distributed across the interface, leading to localized regions where the mechanical properties differ significantly from those of surrounding areas. This heterogeneity, when not adequately quantified, can result in unpredictable behavior under load, potentially compromising the integrity of the structure over time. Therefore, elastic moduli matrix, "weakest vectors", and similarity analysis are conducted to qualify the heterogeneity of the old–new concrete interface.

This section first shows a 6×6 calculated elastic moduli matrix of interface position and non-interface position based on finite element-based numerical homogenization [19,21,29]. As shown in (19), We compare the calculated elastic modulus coefficients with the results from Ref. [19], which reveals similar characteristics in the computed data. Specifically, the matrix exhibits a high degree of alignment, with significantly higher values along the main diagonal. This comparison indirectly supports the validity of the simulation results obtained in this study.

$$\begin{bmatrix} 36.605 & 8.425 & 8.379 & 0.069 & -0.183 & -0.048 \\ 8.425 & 33.015 & 8.216 & 0.022 & -0.024 & -0.018 \\ & & 32.927 & 0.008 & -0.047 & -0.005 \\ & & & 12.571 & -0.046 & -0.027 \\ & \text{Symmetric} & & & 12.517 & 0.005 \\ & & & & & 12.366 \end{bmatrix} \tag{19}$$

As for the results obtained in this study, the elasticity matrix comparison of interface and non-interface highlights significant differences between the non-interface and interface positions in terms of stiffness and anisotropy. In the non-interface region, the diagonal elements exhibit high and uniform values (e.g., $C_{11}$ = 31,937.09, $C_{22}$ = 31,193.96, $C_{33}$ = 35,270.82), indicating greater axial stiffness and isotropic-like behavior due to better compaction and fewer voids. In contrast, the interface region shows lower stiffness in most directions (e.g., $C_{11}$ = 18,970.84, $C_{22}$ = 14,562.60), with notable anisotropy reflected in the relatively high $C_{33}$ = 33,314.93, suggesting directional dependency caused by microstructural defects. Additionally, the off-diagonal elements further reveal differences in shear coupling and anisotropy; the non-interface region exhibits small values close to zero, reflecting minimal coupling and isotropic behavior, whereas the interface region displays greater variability with negative values (e.g., $C_{14} = -26.32$) and higher magnitudes (e.g., $C_{35}$ = 734.93), indicative of internal stresses, localized anisotropy, and weaker bonding. These findings underscore the critical role of microstructural integrity, with non-interface regions being stiffer and more isotropic, while interface regions contribute to compliance and directional dependency due to their inherent weaknesses.

To effectively quantify the anisotropic properties of the concrete interface, this work innovatively proposed and identified the "weakest vector" index based on the research summary of the progress and gap of existing research [2,6,8,9]. These vectors represent directions in which the interface is most susceptible to failure, either due to weaker bonding, higher porosity, or pre-existing cracks. The identification of these weakest vectors is crucial for understanding how the interface will respond to external forces, as regions aligned with these vectors are more likely to experience failure under stress. The "weakest vector" analysis identifies the direction of minimum stiffness in a material by analyzing eigenvalues and eigenvectors of its stiffness matrix. This vector represents the material's weakest response under stress. Visualizing the weakest normal and shear stress directions as distinct arrows highlights the material's directional properties, particularly in anisotropic regions like the old–new concrete interface. The analysis reveals variations in the relative orientation of normal and shear stress components, reflecting the interface's complex stress behavior. This approach provides valuable insights into material anisotropy and stress distribution, enhancing the understanding of structural properties at critical interfaces. By analyzing these vectors, engineers can pinpoint critical regions where localized damage may initiate, thus providing valuable information for optimizing repair strategies and ensuring the long-term durability of the structure.

Once the "weakest vectors" are identified, it becomes necessary to quantify the degree of similarity between different regions of the interface. The similarity analysis of "weakest vectors" reveals the directional properties of the old–new concrete interface [2,34]. By calculating the cosine similarity of these vectors, the analysis quantifies their alignment and homogeneity. The average cosine similarity of 0.62 suggests a relatively high degree of alignment, indicating that the weakest vectors share similar directional tendencies. The weakest normal stress direction and the weakest shear stress direction of each sample are nearly orthogonal, which is physically reasonable. Furthermore, the low variance of 0.11 highlights minimal fluctuation in these alignments, signifying uniformity across samples. Each weakest vector has at least one other vector closely aligned with it, as demonstrated by the high average maximum cosine similarity of 0.99. These findings confirm that the weakest vectors exhibit consistent directional properties, reflecting the anisotropic nature of the interface.

The quantitative analysis of anisotropic properties in the old–new concrete interface requires a nuanced understanding of the directional dependence of the material's mechanical behavior.

Existing studies have demonstrated the existence of anisotropy at the concrete interface [8], but there is a lack of methods to quantify it. Traditional methods often oversimplify this complexity, but by incorporating more advanced techniques [7,16,17], a more accurate representation of the anisotropic nature of the interface can be achieved. These approaches enable a deeper insight into how varying material properties and structural irregularities at the interface influence the overall behavior of the composite material under different loading conditions. Furthermore, the introduction of similarity analysis not only explores the directional characteristics of the weakest vector but also eliminates the randomness of the weakest vector indicator in the calculation results. In other words, similar results are obtained on multiple samples, which can prove the effectiveness and rationality of the "weakest vector" index.

## 4. Conclusions

This study presents a novel framework for quantifying the anisotropic properties and micromechanical behavior of old–new concrete interfaces through X-ray CT and finite element-based numerical homogenization. The results highlight significant anisotropy in the interface, arising from microcracks, voids, and other heterogeneities, which challenge the assumptions of traditional design approaches that rely on homogeneity or empirical reduction factors. By modeling the homogenization of 4-phase concrete materials and generating the elastic moduli matrix, this study identifies the weakest directional vectors, offering a detailed analysis of the interface's heterogeneous properties. These findings provide critical insights into the internal microstructure of concrete, with important implications for improving the design, renovation, and reconstruction of concrete structures.

1. The elasticity matrix highlights significant differences between the interface and non-interface regions of old–new concrete. Non-interface regions exhibit higher axial stiffness (e.g., $C_{11}$ = 31,937.09) and near-isotropic behavior due to better compaction and fewer defects, while interface regions show reduced stiffness (e.g., $C_{11}$ = 18,970.84) and pronounced anisotropy caused by voids and microcracks;
2. Off-diagonal terms in the interface matrix, such as negative values ($C_{14} = -26.32$) and larger magnitudes ($C_{35}$ = 734.93), reflect weaker bonding and irregular stress transfer. These findings underscore the interface's microstructural heterogeneity and directional compliance, which reduce load-bearing capacity and highlight the critical role of anisotropy in interface behavior;

3. The "weakest vectors" at the old–new concrete interface are investigated, representing directions of minimal resistance to normal and shear stress. The average angle of 88.64° between the weakest normal stress and weakest shear stress reflects a predominantly orthogonal relationship with some deviation due to local stress distributions;
4. Cosine similarity analysis reveals higher directional consistency at the interface, with an average similarity of 0.62 compared to 0.23 at non-interface positions, which is consistent with the results observed in X-ray CT images.

**Author Contributions:** Conceptualization, Y.L.; methodology, G.Z. and Y.L.; software, G.Z.; validation, G.Z.; formal analysis, G.Z.; investigation, G.Z.; resources, G.Z.; data curation, G.Z.; writing—original draft preparation, G.Z.; writing—review and editing, Y.L.; visualization, G.Z.; supervision, Y.L.; project administration, Y.L. All authors have read and agreed to the published version of the manuscript.

**Funding:** This research received no external funding.

**Data Availability Statement:** The datasets presented in this article are not readily available because the data are part of an ongoing PhD study. Requests to access the datasets should be directed to guanmingzhang@u.boisestate.edu.

**Conflicts of Interest:** The authors have no conflicts of interest.

## References

1. Brown, R.E.; Willis, H.L. The economics of aging infrastructure. *IEEE Power Energy Mag.* **2006**, *4*, 36–43. [CrossRef]
2. Li, H. Microstructural Quantification, Property Prediction, and Stochastic Reconstruction of Heterogeneous Materials Using Limited X-Ray Tomography Data. Doctoral Dissertation, Arizona State University, Tempe, AZ, USA, 2017.
3. Liu, H.; Zou, H.; Zhang, J.; Zhang, J.; Tang, Y.; Zhang, J.; Xiao, J. Interface bonding properties of new and old concrete: A review. *Front. Mater.* **2024**, *11*, 1389785. [CrossRef]
4. Zhang, J.; Li, J.; Zhao, Y.; Wang, S.; Guan, Z. Concrete Cover Cracking and Reinforcement Corrosion Behavior in Concrete with New-to-Old Concrete Interfaces. *Materials* **2023**, *16*, 5969. [CrossRef]
5. Golewski, G.L. The phenomenon of cracking in cement concretes and reinforced concrete structures: The mechanism of cracks formation, causes of their initiation, types and places of occurrence, and methods of detection—A review. *Buildings* **2023**, *13*, 765. [CrossRef]
6. Kayondo, M.; Combrinck, R.; Boshoff, W.P. State-of-the-art review on plastic cracking of concrete. *Constr. Build. Mater.* **2019**, *225*, 886–899. [CrossRef]
7. Zhang, T.; Rahman, M.A.; Peterson, A.; Lu, Y. Novel Damage Index-Based Rapid Evaluation of Civil Infrastructure Subsurface Defects Using Thermography Analytics. *Infrastructures* **2022**, *7*, 55. [CrossRef]
8. Aaleti, S.; Sritharan, S. Quantifying bonding characteristics between UHPC and normal-strength concrete for bridge deck application. *J. Bridge Eng.* **2019**, *24*, 04019041. [CrossRef]
9. Austin, S.; Robins, P.; Pan, Y. Shear bond testing of concrete repairs. *Constr. Build. Mater.* **1999**, *13*, 249–258. [CrossRef]
10. Bentz, D.P.; De la Varga, I.; Muñoz, J.F.; Spragg, R.P.; Graybeal, B.A.; Hussey, D.S.; Jacobson, D.L.; Jones, S.Z.; LaManna, J.M. Influence of substrate moisture state and roughness on interface microstructure and bond strength: Slant shear vs. pull-off testing. *Constr. Build. Mater.* **2020**, *235*, 117491. [CrossRef]
11. Beushausen, H.; Höhlig, B.; Talotti, M. The influence of substrate moisture preparation on bond strength of concrete overlays and the microstructure of the OTZ. *Cem. Concr. Res.* **2016**, *91*, 2–11. [CrossRef]
12. Carbonell Muñoz, M.A.; Harris, D.K.; Ahlborn, T.M.; Froster, D.C. Bond performance between ultrahigh-performance concrete and normal-strength concrete. *J. Mater. Civ. Eng.* **2014**, *26*, 04014023. [CrossRef]
13. Courard, L.; Piotrowski, T.; Garbacz, A. Near-to-surface properties affecting bond strength in concrete repair. *Constr. Build. Mater.* **2014**, *65*, 496–505. [CrossRef]
14. Diab, A.M.; Abd Elmoaty, A.M.; Tag Eldin, M.R. Slant shear bond strength between self-compacting concrete and old concrete. *Constr. Build. Mater.* **2020**, *234*, 117387. [CrossRef]
15. Xiao, J.; Li, W.; Corr, D.J.; Shah, S.P. Effects of interfacial transition zones on the stress-strain behavior of modeled recycled aggregate concrete. *Cem. Concr. Res.* **2013**, *52*, 82–99. [CrossRef]
16. Boukhatem, B.; Kenai, S.; Tagnit-Hamou, A.; Ghrici, M. Application of new information technology on concrete: An overview. *J. Civ. Eng. Manag.* **2011**, *17*, 248–258. [CrossRef]

17. Vicente, M.A.; González, D.C.; Mínguez, J. Recent advances in the use of computed tomography in concrete technology and other engineering fields. *Micron* **2019**, *118*, 22–34. [CrossRef] [PubMed]
18. Fukuda, D.; Nara, Y.; Kobayashi, Y.; Maruyama, M.; Koketsu, M.; Hayashi, D.; Kaneko, K. Investigation of self-sealing in high-strength and ultra-low-permeability concrete in water using micro-focus X-ray CT. *Cem. Concr. Res.* **2012**, *42*, 1494–1500. [CrossRef]
19. Luo, Q.; Liu, D.; Qiao, P.; Zhou, Z.; Zhao, Y.; Sun, L. Micro-CT-based micromechanics and numerical homogenization for effective elastic property of ultra-high performance concrete. *Int. J. Damage Mech.* **2020**, *29*, 45–66. [CrossRef]
20. Wang, R.; Wu, H.; Zhao, M.; Liu, Y.; Chen, C. The classification and mechanism of microcrack homogenization research in cement concrete based on X-ray CT. *Buildings* **2022**, *12*, 1011. [CrossRef]
21. Sanahuja, J.; Toulemonde, C. Numerical homogenization of concrete microstructures without explicit meshes. *Cem. Concr. Res.* **2011**, *41*, 1320–1329. [CrossRef]
22. Moharekpour, M.; Liu, P.; Schmidt, J.; Oeser, M.; Jing, R. Evaluation of design procedure and performance of continuously reinforced concrete pavement according to AASHTO design methods. *Materials* **2022**, *15*, 2252. [CrossRef]
23. *ASTM C94/C94M-24c*; Standard Specification for Ready-Mixed Concrete. ASTM International: West Conshohocken, PA, USA, 2024.
24. *ASTM C150/C150M-20*; Standard Specification for Portland Cement. ASTM International: West Conshohocken, PA, USA, 2020.
25. *ASTM C143/C143M-20*; Standard Test Method for Slump of Hydraulic-Cement Concrete. ASTM International: West Conshohocken, PA, USA, 2020.
26. du Plessis, A.; Boshoff, W.P. A review of X-ray computed tomography of concrete and asphalt construction materials. *Constr. Build. Mater.* **2019**, *199*, 637–651. [CrossRef]
27. Denisiewicz, A.; Kuczma, M.; Kula, K.; Socha, T. Influence of boundary conditions on numerical homogenization of high performance concrete. *Materials* **2021**, *14*, 1009. [CrossRef]
28. Lu, Y.; Garboczi, E.J. Bridging the gap between random microstructure and 3D meshing. *J. Comput. Civ. Eng.* **2014**, *28*, 04014007. [CrossRef]
29. Wu, T.; Temizer, I.; Wriggers, P. Computational thermal homogenization of concrete. *Cem. Concr. Compos.* **2013**, *35*, 59–70. [CrossRef]
30. Mercier, S.; Molinari, A. Homogenization of elastic–viscoplastic heterogeneous materials: Self-consistent and Mori-Tanaka schemes. *Int. J. Plast.* **2009**, *25*, 1024–1048. [CrossRef]
31. Feng, Y.; Yong, H.; Zhou, Y. A concurrent multiscale framework based on self-consistent clustering analysis for cylinder structure under uniaxial loading condition. *Compos. Struct.* **2021**, *266*, 113827. [CrossRef]
32. Jiang, D. Stress, Strain, and Elasticity. In *Continuum Micromechanics: Theory and Application to Multiscale Tectonics*; Springer: Cham, Switzerland, 2023; pp. 57–96.
33. Deng, F.; Xu, L.; Cao, C.; Chi, Y. Effect of cellulose nanofiber addition on the microstructure characterization and nano-mechanical behavior of interfacial transition zones in recycled concrete. *J. Mater. Res. Technol.* **2024**, *33*, 7572–7585. [CrossRef]
34. Nemat-Nasser, S.; Lori, M.; Datta, S.K. Micromechanics: Overall Properties of Heterogeneous Materials. *ASM J. Appl. Mech.* **1996**, *63*, 561. [CrossRef]

**Disclaimer/Publisher's Note:** The statements, opinions and data contained in all publications are solely those of the individual author(s) and contributor(s) and not of MDPI and/or the editor(s). MDPI and/or the editor(s) disclaim responsibility for any injury to people or property resulting from any ideas, methods, instructions or products referred to in the content.